SIAM J. APPL. MATH.
Vol. 72, No. 4, pp. 1149–1168

DEPTH AVERAGED ANALYTIC SOLUTION FOR A LAMINAR FLOW FUEL CELL WITH ELECTRIC DOUBLE LAYER EFFECTS*

ISAAC B. SPRAGUE† AND PRASHANTA DUTTA†

Abstract. A comprehensive multidimensional analysis is presented for a laminar flow fuel cell with electric double layer (EDL) dependent kinetics in a planar microdevice. The EDL is described with the Stern model, and a generalized Frumkin–Butler–Volmer (gFBV) equation is used to describe the EDL dependent kinetics. The liquid electrolyte is modeled with the Poisson–Nernst–Planck (PNP) equations and the incompressible Navier–Stokes (NS) equations. For planar microchannel applications, the three-dimensional model is reduced to an in-plane depth averaged set of equations through an asymptotic analysis. The diffuse layers are resolved in the thin double layer limit through asymptotic matching by considering the Debye length to channel width ratio as a smallness parameter. This yields an outer problem for the bulk electrolyte and an inner problem for the anode and cathode diffuse regions. Fuel cell performance is then evaluated by introducing several specified local current density profiles. The resulting approximate analytic expressions, based on the proposed specified current density profiles, are validated against results from a numerical solution of the full in-plane PNP–NS–gFBV model, in which a priori current profile approximations are not required. We demonstrate that simple current density profiles yield physically unrealistic electrode potential distributions despite producing reasonably accurate overall device performance results. We also present an appropriate current density profile which yields accurate spatial distributions for the continuum fields and electrode potential distributions.

Key words. laminar flow fuel cell, depth averaged shallow microchannel, electric double layer kinetics

AMS subject classifications. 76D05, 76D08

DOI. 10.1137/110843113

1. Introduction.

Fuel cells are highly complex electrochemical systems that defy understanding through empirical studies alone, and mathematical models are therefore critical to thoroughly investigate the underlying physics. There exist a number of mathematical models to study fuel cells [1, 2], and the presented theoretical studies can be roughly divided into two groups—numerical simulations and analytic solutions. Both approaches have benefits and drawbacks. Numerical simulations of fuel cells are extremely flexible and can account for a wide variety of phenomena. However, this can lead to a convoluted model with a high cost of implementation as well as require access to proprietary source codes. On the other hand, analytic solutions are immediately accessible to a wider range of researchers but can only address simplified problems and geometry.

In fuel cells the electrochemical reactions proceed in the presence of the electric double layer (EDL) as charge is transferred between the electrode and electrolyte, forming the basis of electrode kinetics and fuel cell operation [3]. The EDL is a microscopic area immediately adjacent to the electrode where a charge density develops in the electrolyte. The codependency between the electrolyte potential and ion transport (and thus the EDL) can be described with the Poisson–Nernst–Planck (PNP) equations and the EDL dependent electrode kinetics with the generalized Frumkin–Butler–Volmer (gFBV) equation [4]. The PNP–gFBV equations have been used to

*Received by the editors August 2, 2011; accepted for publication (in revised form) May 30, 2012; published electronically August 15, 2012.
http://www.siam.org/journals/siap/72-4/84311.html
†School of Mechanical and Materials Engineering, Washington State University, Pullman, WA 99164-2920 (isaac.sprague@email.wsu.edu, dutta@mail.wsu.edu).

investigate EDL effects on electrode kinetics in electrochemical cells [5, 6, 7]. They have also been successfully applied to specifically study the EDL in the context of fuel cells [8, 9, 10, 11, 12].

For most practical fuel cell problems, the EDL satisfies the *thin double layer* condition in which the EDL thickness is much less than the electrode separation. In this case, an approximate but accurate analytic solution to the PNP equations can be obtained using asymptotic analysis [13, 14], which has been used to investigate many novel kinetic behaviors [15, 16, 17]. However, all of these analyses are based on only one spatial dimension. A single dimensional analysis is not sufficient to study the operating behavior of fuel cells which are inherently multidimensional systems where the conditions at the reaction plane vary along the electrodes (e.g., formation of depletion boundary layers). Therefore, a multidimensional analysis is needed. Thus, the goal of this work is to develop a multidimensional analytic solution for a laminar flow fuel cell (LFFC) with EDL effects. To accomplish this we employ the method of matched asymptotic expansions to resolve the model into a set of near wall EDL phenomena (inner) regions and a bulk electrolyte (outer) region. We solve the inner problem by adjusting existing solutions [13] to the multidimensional problem. The outer problem becomes a convection-diffusion problem akin to Leveque's classic problem with reactions. Similar convection-diffusion-reaction problems have been solved for different systems, such as electrodialysis [18].

Existing one-dimensional analytic analyses of electrochemical cells specify the electrode current density at the problem onset (i.e., galvanostatic operation). While this simplifies the analysis, it requires the local current density to be known a priori. In a multidimensional device, the current distribution along the fuel cell varies to maintain constant anode and cathode potentials in the metallic electrodes. Therefore, we include in our analysis different specified local current density profiles along the electrodes and arrive at an appropriate local current density profile that accurately describes the total device behavior and continuum distributions of various control parameters. We then study how the profile is affected by changing fuel cell operating conditions.

The rest of the article is organized as follows. The basic theory is developed in section 2, including the mathematical model. The main simplifying assumptions and their justifications are provided in section 3. Then, in section 4 we develop an analytic approximate solution with general local current density profiles. In section 5 we replace these general profiles with different specified local current density profiles completing the solution. These profiles are then used to evaluate cell potential and device performance (section 6) and finally the spatial distribution of the physical quantities in an LFFC (section 7).

2. Theory. In this section we present the full mathematical model for an LFFC. We chose the LFFC because its simple membraneless architecture allows for a straightforward analysis while still maintaining relevance to the fuel cell community (e.g., the liquid electrolyte does not require the more complicated transport description that membrane electrolytes need [19]). LFFCs were first presented early in the last decade and have been studied experimentally [20, 21, 22] and numerically [23, 24, 25]. The present LFFC consists of a shallow microchannel as shown in Figure 2.1 with a channel width of $0 \leq y \leq w$ and a height of $0 \leq z \leq d$ such that $d \ll w$. The main channel is fed by two inlet channels—one for fuel and the other for oxidant. The continuum domain is semi-infinite, beginning where the inlets merge into the single main channel and bounded by the reaction planes at the electrodes (i.e., the interface between

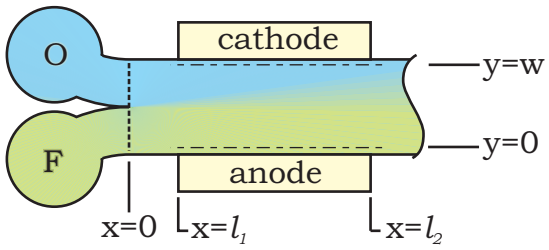

FIG. 2.1. *Schematic of an LFFC in a shallow microchannel showing the in-plane cross-section. The channel depth in the vertical axis is defined from $z = 0$ to $z = d$. There are an inlet for fuel and an inlet for oxidant. The semi-infinite continuum domain begins where the inlets meet at $x = 0$ and is bounded by the anode and cathode reaction planes at $y = 0$ and $y = w$, respectively. The electrodes span a finite distance along the walls from $x = l_1$ to $x = l_2$.*

the Stern and diffuse layers). The electrodes span a finite distance ($l_1 \leq x_{\mathrm{EL}} \leq l_2$) along the channel walls, and the chemical reactions take place only at the electrode-electrolyte interface. The inlet reactant streams consist of a reactant-electrolyte solution, and for the purpose of this work we consider a simple binary electrolyte consisting of a cation (C^+) and an anion (A^-) of unit charge $z_+ = -z_- = 1$. To maintain generality of the analysis, the overall device reaction is formulated in terms of general chemical species such as fuel (F), oxidant (O), and waste. The overall device reaction can be presented as

$$S_F \cdot F + S_O \cdot O \rightarrow W_F + W_O, \tag{2.1}$$

where W_F, W_O are the waste species from the fuel oxidation and oxidant reduction reactions, respectively. Since the purpose of the present analysis is to study EDL effects, the waste terms are omitted from the rest of the analysis. The stoichiometric coefficients S_F, S_O are determined by the specific reaction, and for this analysis we assume them to be unity. By splitting the overall reaction into the appropriate half reactions for fuel oxidation and oxidant reduction we get, respectively,

$$\begin{aligned} S_F \cdot F &\underset{k'_F}{\overset{k_F}{\longleftrightarrow}} S_{C^+} \cdot C^+ + n \cdot e^- + W_F, \\ S_{C^+} \cdot C^+ + n \cdot e^- + S_O \cdot O &\underset{k'_O}{\overset{k_O}{\longleftrightarrow}} W_O, \end{aligned} \tag{2.2}$$

where n is the number of electrons (e^-) involved in the reaction. Each half reaction is allowed to proceed in either direction as determined by the forward and reverse rate constants k, k', respectively. In (2.2) we have taken the cation as the working ion, produced by fuel oxidation and consumed by oxidant reduction. The anion is inert and does not participate in the electrode reactions.

2.1. Electrolyte. The electrolyte phase in the continuum domain is described by the PNP equations. The net flux density of a specific species is the sum of the advection, diffusion, and migration flux densities and is given by

$$\vec{N}_i = \vec{v} c_i - D_i \nabla c_i - z_i \omega_i F c_i \nabla \phi_E, \tag{2.3}$$

where c_i is the species concentration, D_i is the diffusion coefficient, ω_i is the ionic mobility, and the subscript $i = F, O, C^+, A^-$ indicates the species considered. The

remaining terms are the bulk fluid velocity ($\overrightarrow{v}$), Faraday's constant (F), and the electrolyte potential (ϕ_E). The concentration distributions are then given by the steady-state Nernst–Planck equations,

$$\nabla \cdot \overrightarrow{N}_i = 0, \tag{2.4}$$

and the electrolyte potential can be related to the ion concentration distribution by the electrostatic Poisson equation,

$$-\nabla \cdot (\varepsilon_E \nabla \phi_E) = F \sum z_i c_i, \tag{2.5}$$

where ε_E is the electrolyte permittivity. The bulk flow of the electrolyte stream is given by the incompressible steady-state Navier–Stokes (NS) and continuity equations,

$$\rho_v \left(\overrightarrow{v} \cdot \nabla\right) \overrightarrow{v} = \nabla \cdot (\mu_v \nabla \overrightarrow{v}) - \nabla p - F \nabla \phi_E \sum z_i c_i, \tag{2.6}$$

$$\nabla \cdot (\rho_v \overrightarrow{v}) = 0, \tag{2.7}$$

where ρ_v and μ_v are the fluid density and viscosity and p is pressure.

2.2. Electrode kinetics and boundary conditions. The PNP–NS model (2.4)–(2.7) only describes the LFFC throughout the continuum domain which extends from the anode to cathode reaction planes. Descriptions for the Stern layer and electrode kinetics are still needed to capture the boundary effects. The Stern model is used to describe the inner portion of the EDL, and the Stern potential can be expressed by

$$\phi_S = \lambda_S \left.\frac{\partial \phi_E}{\partial \overrightarrow{n}}\right|_{\text{Reaction Plane}} = \psi_{\text{EL}} - \phi_E|_{\text{Reaction Plane}}, \tag{2.8}$$

where $\vec{n}$ is the unit normal to the electrode surface and λ_S is the Stern layer thickness. The Stern potential is also the difference between the electrolyte potential (ϕ_E) at the reaction plane and the electrode potential (ψ_{EL}). The subscript EL can refer to either the anode or cathode electrode. Equation (2.8) can be used as a boundary condition for the Poisson equation [13, 15, 16]. The electrode reactions are assumed to occur only at the reaction plane and can be applied as a boundary condition for the Nernst–Planck equations by relating the net species flux to the local current density at the electrode ($j_{\text{EL}}(x)$):

$$\left.\overrightarrow{N}_i \cdot \overrightarrow{n}\right|_{\text{Reaction Plane}} = \frac{S_i \, j_{\text{EL}}(x)}{nF}. \tag{2.9}$$

The local current density can then be related to the reaction rate of the half reactions (see (2.2)) which is given by the gFBV equation,

$$\begin{aligned} j_F &= Fn\left[k_F c_F \exp\left(\frac{(1-\beta)\, z_+ F}{RT}\phi_S\right) - k'_F c_{C^+} \exp\left(-\frac{\beta z_+ F}{RT}\phi_S\right)\right], \\ j_O &= Fn\left[k'_O \exp\left(\frac{(1-\beta)\, z_+ F}{RT}\phi_S\right) - k_O c_O c_{C^+} \exp\left(-\frac{\beta z_+ F}{RT}\phi_S\right)\right], \end{aligned} \tag{2.10}$$

for fuel oxidation and oxidant reduction, respectively. R is the universal gas constant and T is absolute temperature. The reactant concentrations are taken at the reaction

plane. The parameter β is a kinetics symmetry factor and is assumed to be $1/2$ for all of the results presented in this work. No reaction occurs along the insulating channel walls, and the boundary conditions here are therefore

$$\left.\frac{\partial \phi_E}{\partial \overrightarrow{n}}\right|_{\text{Wall}} = 0, \quad \left.\overrightarrow{N}_i \cdot \overrightarrow{n}\right|_{\text{Wall}} = 0. \tag{2.11}$$

Finally, the boundary conditions at the channel inlet where the concentrations are specified are

$$\begin{gathered} c_{C^+}(0,y,z) = c_{\text{in}}, \quad c_{A^-}(0,y,z) = c_{\text{in}}, \quad \left.\frac{\partial \phi_E}{\partial \overrightarrow{n}}\right|_{\text{Inlet}} = 0, \\ c_F(0,y,z) = \begin{cases} c_{\text{in}}, & 0 \le y \le w/2, \\ 0, & w/2 < y \le w, \end{cases} \qquad c_O(0,y,z) = \begin{cases} 0, & 0 \le y \le w/2, \\ c_{\text{in}}, & w/2 < y \le w. \end{cases} \end{gathered} \tag{2.12}$$

For the bulk flow we assume a fully developed profile at the channel inlet and the no-slip and no-penetration conditions along the channel walls and electrodes.

2.3. Dimensionless equations. We now introduce the dimensionless variables $C_E \equiv (c_+ + c_-)/2c_{\text{in}}$, $\rho_E \equiv (c_+ - c_-)/2c_{\text{in}}$, and $\Phi_E \equiv \phi_E z_+ F/RT$ for (average) electrolyte concentration, charge density, and electrolyte potential, respectively. The Nernst–Planck equations for anions and cations result in the following dimensionless equations for electrolyte concentration and charge density:

$$\frac{\partial}{\partial Z}\left(\frac{\partial C_E}{\partial Z} + \rho_E \frac{\partial \Phi_E}{\partial Z}\right) = \epsilon_Z \left(\overrightarrow{V} \cdot \nabla C_E - \nabla_2^2 C_E - \nabla_2 \cdot (\rho_E \nabla_2 \Phi_E)\right), \tag{2.13}$$

$$\frac{\partial}{\partial Z}\left(\frac{\partial \rho_E}{\partial Z} + C_E \frac{\partial \Phi_E}{\partial Z}\right) = \epsilon_Z \left(\overrightarrow{V} \cdot \nabla \rho_E - \nabla_2^2 \rho_E - \nabla_2 \cdot (C_E \nabla_2 \Phi_E)\right), \tag{2.14}$$

where the streamwise and cross-stream spatial coordinates have been scaled by the channel width w ($X \equiv x/w$, $Y \equiv y/w$, $L_1 \equiv l_1/w$, $L_2 \equiv l_2/w$) and the depth coordinate has been scaled by the channel depth d ($Z \equiv z/d$). Note that we have also defined a smallness parameter in terms of the channel aspect ratio as $\epsilon_Z \equiv (d/w)^2$. This is analogous to the smallness parameter used in lubrication theory, and the asymptotic analysis that follows can be thought of as an application of the lubrication approximation to a fuel cell model. Additionally, it has been assumed that the diffusion coefficients are equivalent for both ions ($D_+ = D_- = D_E$). The in-plane velocity, $\overrightarrow{V}_2 = (V_X, V_Y)$, has been scaled as ($\overrightarrow{V}_2 \equiv \overrightarrow{v}_2 w/D_E$), and the vertical velocity V_Z scale has been set such that all of the terms in the continuity equation (2.7) are of the same order. For convenience we have also defined the in-plane gradient as $\nabla_2 = (\partial/\partial X, \partial/\partial Y)$.

The neutral species are scaled by the specified inlet concentration c_{in} ($C_F \equiv c_F/c_{\text{in}}$, $C_O \equiv c_O/c_{\text{in}}$), and the dimensionless Nernst–Planck equation for the neutral species is

$$\alpha \frac{\partial^2 C_i}{\partial Z^2} = \epsilon_Z \left(\overrightarrow{V} \cdot \nabla C_i - \alpha \nabla_2^2 C_i\right), \tag{2.15}$$

where α is the ratio between the diffusion coefficients of the neutral species and electrolyte ions, $\alpha = D_F/D_E = D_O/D_E$, and the ion diffusion coefficient is $D_E =$

$\omega_E RT$. We have also redefined the subscript i to refer only to the neutral species; $i = F, O$. The dimensionless Poisson's equation can also be written

$$-{\epsilon_D}^2 \frac{\partial^2 \Phi_E}{\partial Z^2} = \epsilon_Z \left({\epsilon_D}^2 \nabla_2^2 \Phi_E + \rho_E \right), \tag{2.16}$$

where $\epsilon_D \equiv \lambda_D / w$ is the scaled Debye length ($\lambda_D = \sqrt{(\frac{\varepsilon_E RT}{2z_+^2 F^2 c_0})}$). Finally, dimensionless pressure is defined as $P \equiv pd^2/\mu_v D_E$, and the dimensionless in-plane and vertical NS equations are

$$\frac{\partial^2 \overrightarrow{V}_2}{\partial^2 Z} - \nabla_2 P = \epsilon_Z \left(Sc^{-1} \overrightarrow{V} \cdot \nabla \overrightarrow{V}_2 - \nabla_2^2 \overrightarrow{V}_2 + 2\Gamma \rho_E \nabla_2 \Phi_E \right), \tag{2.17}$$

$$-\frac{\partial P}{\partial Z} = {\epsilon_Z}^2 \left(Sc^{-1} \overrightarrow{V} \cdot \nabla V_Z - \nabla_2^2 V_Z \right) + \epsilon_Z \left(-\frac{\partial^2 V_Z}{\partial^2 Z} + 2\Gamma \rho_E \frac{\partial \Phi_E}{\partial Z} \right), \tag{2.18}$$

respectively, where $Sc = \mu_v / \rho_v D_E$ is the Schmidt number. The dimensionless parameter for the electrostatic body force term is $\Gamma = C_E w^2 / \mu_v \omega_E$.

3. Simplifying assumptions. To obtain an analytic solution to the model problem we must simplify the full PNP–NS model. The main simplifying assumptions in the present analysis are as follows.

1. The flow field is fully developed yielding $\partial \overrightarrow{V} / \partial X = 0$, $V_Y = 0$, $V_Z = 0$.

2. The electrostatic body force term in the NS equations (2.17) and (2.18) is negligible. This has been shown to be valid in an LFFC [10].

3. The microchannel is shallow (i.e., $d \ll w$ and therefore ϵ_Z is small). This holds true in several experimental studies of LFFCs [26, 27, 28, 29].

4. The EDLs satisfy the thin double layer condition (i.e., $\lambda_D \ll w$ and therefore ϵ_D is small). This holds because the Debye length is on the order of nanometers, while the channel width is on the order of a millimeter.

5. The device Peclet number ($Pe = U_0/\alpha$ for neutral species and $Pe_E = U_0$ for the electrolyte) is sufficiently large that reactant crossover does not occur ($Pe \geq 10$). Thus only fuel oxidation occurs at the anode and oxidant reduction at the cathode, and mixed potentials need not be included [11].

6. Advection is the dominant flux in the streamwise direction, and therefore the diffusion flux in the streamwise direction is negligible. This is valid for the practical device Peclet numbers required to prevent reactant crossover [30].

Note. Assumptions 1 and 4 are similar to those made in previous convection-diffusion-reaction solutions [18] except that we have allowed current density to vary along the channel axis.

3.1. Shallow channel assumption and the depth averaged equations. We now implement assumptions 1 and 2 as well as introduce the asymptotic expansion $f_i(X,Y,Z) \sim \grave{f}_i(X,Y,Z) = \grave{f}_i^0(X,Y,Z) + \epsilon_Z \grave{f}_i^1(X,Y,Z) + O\left({\epsilon_Z}^2\right)$ into (2.13)–(2.18) and take the resulting leading order (${\epsilon_Z}^0$) set of equations, which yields

$$\frac{\partial}{\partial Z} \left(\frac{\partial \grave{C}_E^0}{\partial Z} + \grave{\rho}_E^0 \frac{\partial \grave{\Phi}_E^0}{\partial Z} \right) = 0, \tag{3.1}$$

$$\frac{\partial}{\partial Z} \left(\frac{\partial \grave{\rho}_E^0}{\partial Z} + \grave{C}_E^0 \frac{\partial \grave{\Phi}_E^0}{\partial Z} \right) = 0, \tag{3.2}$$

$$\alpha \frac{\partial^2 \grave{C}_i^0}{\partial Z^2} = 0, \tag{3.3}$$

$$-{\epsilon_D}^2 \frac{\partial^2 \grave{\Phi}_E^0}{\partial Z^2} = 0, \tag{3.4}$$

$$\frac{\partial^2 \grave{V}_X^0}{\partial^2 Z} = \frac{\partial \grave{P}^0}{\partial X}, \tag{3.5}$$

$$\frac{\partial \grave{P}^0}{\partial Y} = 0, \quad \frac{\partial \grave{P}^0}{\partial Z} = 0. \tag{3.6}$$

From (3.4), it has been found that the leading order electrolyte potential is independent of the vertical coordinate ($\grave{\Phi}_E^0 = \grave{\Phi}_E^0(X,Y)$). Moreover, using this and (3.1) and (3.2), we can show that the leading order charge density and concentrations are also independent of the vertical coordinate: $\grave{\rho}_E^0 = \grave{\rho}_E^0(X,Y)$, $\grave{C}_i^0 = \grave{C}_i^0(X,Y)$, $\grave{C}_E^0 = \grave{C}_E^0(X,Y)$. To make these conclusions we have also used the no-flux and insulating conditions at the top and bottom walls (see (2.11)). The leading order Y- and Z-momentum equations (3.6) give that pressure is a function of the streamwise coordinate only: $\grave{P}^0 = \grave{P}^0(X)$. This along with the leading order X-momentum equation (3.5) gives a streamwise velocity profile that is parabolic in the vertical coordinate only ($\grave{V}_X^0(Z) = 4U_M\left[Z - Z^2\right]$), where U_M is the maximum dimensionless velocity. The leading order in-plane governing equations are obtained by first taking the ${\epsilon_Z}^1$-order system of equations from (2.13)–(2.16) and introducing the depthwise average $\overline{f} = \int_0^1 f dZ$ [31] to eliminate the depth coordinate dependency. Using the insulating and no-flux boundary conditions (2.11) and dropping the accent and superscript results in the leading order depthwise averaged equations

$$U_0 \frac{\partial C_E}{\partial X} = \frac{\partial}{\partial X}\left(\frac{\partial C_E}{\partial X} + \rho_E \frac{\partial \Phi_E}{\partial X}\right) + \frac{\partial}{\partial Y}\left(\frac{\partial C_E}{\partial Y} + \rho_E \frac{\partial \Phi_E}{\partial Y}\right), \tag{3.7}$$

$$U_0 \frac{\partial \rho_E}{\partial X} = \frac{\partial}{\partial X}\left(\frac{\partial \rho_E}{\partial X} + C_E \frac{\partial \Phi_E}{\partial X}\right) + \frac{\partial}{\partial Y}\left(\frac{\partial \rho_E}{\partial Y} + C_E \frac{\partial \Phi_E}{\partial Y}\right), \tag{3.8}$$

$$U_0 \frac{\partial C_i}{\partial X} = \alpha\left(\frac{\partial^2 C_i}{\partial^2 X} + \frac{\partial^2 C_i}{\partial^2 Y}\right), \tag{3.9}$$

$$-{\epsilon_D}^2\left(\frac{\partial^2 \Phi_E}{\partial^2 X} + \frac{\partial^2 \Phi_E}{\partial^2 Y}\right) = \rho_E \tag{3.10}$$

for electrolyte concentration, charge density, fuel, oxidant, and electrolyte potential, where $U_0 = 2U_M/3$. Introducing dimensionless current $J = jw/(4nFD_E c_0)$, the boundary conditions for (3.7)–(3.9) can be written for $Y = 0$, $Y = 1$, and $X = 0$, respectively:

$$\begin{gathered}\frac{\partial C_E}{\partial Y} + \rho_E \frac{\partial \Phi_E}{\partial Y} = -2S_{C^+} J_{\mathrm{AN}}(X), \quad \frac{\partial \rho_E}{\partial Y} + C_E \frac{\partial \Phi_E}{\partial Y} = -2S_{C^+} J_{\mathrm{AN}}(X), \\ \alpha \frac{\partial C_F}{\partial Y} = 4J_{\mathrm{AN}}(X), \quad \alpha \frac{\partial C_O}{\partial Y} = 0,\end{gathered} \tag{3.11}$$

$$\begin{gathered}\frac{\partial C_E}{\partial Y} + \rho_E \frac{\partial \Phi_E}{\partial Y} = 2S_{C^+} J_{\mathrm{CA}}(X), \quad \frac{\partial \rho_E}{\partial Y} + C_E \frac{\partial \Phi_E}{\partial Y} = 2S_{C^+} J_{\mathrm{CA}}(X), \\ \alpha \frac{\partial C_F}{\partial Y} = 0, \quad \alpha \frac{\partial C_O}{\partial Y} = 4J_{\mathrm{CA}}(X),\end{gathered} \tag{3.12}$$

$$C_E = 1, \quad \rho_E = 0,$$

$$C_F = \begin{cases} 1, & Y \leq 1/2, \\ 0, & Y > 1/2, \end{cases} \qquad C_O = \begin{cases} 0, & Y \leq 1/2, \\ 1, & Y > 1/2. \end{cases} \tag{3.13}$$

The electrolyte potential boundary conditions can be written from the dimensionless Stern model and, assuming that the channel inlet is electrically insulating,

$$\Phi_S = \epsilon_D \delta \left. \frac{\partial \Phi_E}{\partial \overrightarrow{n}} \right|_{\text{Reaction Plane}}, \quad \frac{\partial \Phi_E}{\partial X}(0, Y) = 0, \tag{3.14}$$

where $\delta = \lambda_S / \lambda_D$ is the Stern layer width to Debye length ratio and is a measure of the ionic strength of the electrolyte.

4. Analysis. In this section we develop an analytical solution for an LFFC described by the reduced model presented in (3.7)–(3.10) and the boundary conditions presented in (3.11)–(3.14). Our approach is to use asymptotic matching and seek leading order approximations for electrolyte concentration, charge density, and electrolyte potential distributions. The method of matched asymptotic expansions works by separating the problem into inner and outer regions and matching the resulting solutions. For the present analysis we use asymptotic matching at both electrodes effectively separating the domain into three regions—the bulk electrolyte and the anode and cathode diffuse layers. The neutral species distributions are not influenced by the EDL, and therefore we only need to consider them in the bulk region. It should be pointed out that the asymptotic approximation breaks down at leading order for conditions when the electrolyte concentration in the bulk region is fully depleted at the cathode [16]. For static electrolytes, this corresponds to cells operating near the classical limiting current. However, for the flowing electrolyte of an LFFC, it is unlikely that the device presented would operate under such conditions.

The final analytical expressions are compared with numerical results. For the numerical results the full PNP–gFBV model (2.3)–(2.12) is solved using an in-house numerical simulation. The numerical simulation is capable of resolving the full model throughout the continuum domain without the need for inner and outer solutions. The details of the numerical model are presented elsewhere [10] and will not be repeated.

4.1. Bulk region. We start by introducing the asymptotic expansion (where the $\hat{}$ accent denotes the asymptotic approximation in the outer region) $f(X,Y) \sim \hat{f}(X,Y) = \hat{f}^0(X,Y) + \epsilon_D \hat{f}^1(X,Y) + O\left({\epsilon_D}^2\right)$. The leading order $({\epsilon_D}^0)$ outer region problem for electrolyte concentration, electrolyte potential, and charge density then becomes

$$U_0 \frac{\partial \hat{C}_E^0}{\partial X} = \frac{\partial^2 \hat{C}_E^0}{\partial {Y^2}}, \tag{4.1}$$

$$\frac{\partial}{\partial X}\left(\hat{C}_E^0 \frac{\partial \widehat{\Phi}_E^0}{\partial X}\right) + \frac{\partial}{\partial Y}\left(\hat{C}_E^0 \frac{\partial \widehat{\Phi}_E^0}{\partial Y}\right) = 0, \tag{4.2}$$

$$\widehat{\rho}_E^0 = 0. \tag{4.3}$$

Note. We have also implemented assumption 4.

4.1.1. Bulk concentration distributions. From (4.3), the bulk electrolyte region is considered to be electrically neutral, decoupling the ionic transport from the electrolyte potential. The resulting outer problem for the electrolyte concentration

TABLE 4.1
Specific boundary condition functions for the various concentration distributions in the general solution in (4.6).

	$F_{X=0}(Y)$	$F_{Y=0}(X)$	$F_{Y=1}(X)$
Fuel, C_F	$1, \quad Y \le 1/2$ $0, \quad Y > 1/2$	$\frac{-4J_{\mathrm{AN}}(X)}{\alpha}$	0
Oxidant, C_O	$0, \quad Y \le 1/2$ $1, \quad Y > 1/2$	0	$\frac{4J_{\mathrm{CA}}(X)}{\alpha}$
Electrolyte, $\hat{C}_E^0$	1	$\frac{2S_{C^+}J_{\mathrm{AN}}(X)}{\alpha}$	$\frac{2S_{C^+}J_{\mathrm{CA}}(X)}{\alpha}$

(4.1) is therefore equivalent to the neutral species transport equation (3.9) with $\alpha = 1$ (and no streamwise diffusion). Therefore, we only need to seek a single solution for a general case,

$$U_0 \frac{\partial C_i}{\partial X} = \alpha \frac{\partial^2 C_i}{\partial^2 Y}, \tag{4.4}$$

with boundary conditions

$$-\frac{\partial C_i}{\partial Y}(X,0) = F_{Y=0}(X), \quad \frac{\partial C_i}{\partial Y}(X,1) = F_{Y=1}(X), \tag{4.5}$$
$$C_i(0,Y) = F_{X=0}(Y).$$

Our next step is to solve (4.4) with boundary conditions (4.5) using the integral transform technique [30, 32], which yields the general concentration distribution

$$C_i(X,Y) = \sum_{p=0}^{\infty} \left(\frac{H(\gamma_p, Y)}{N(\gamma_p)} \exp\left[-\left(\frac{\alpha}{U_0}\right)\gamma_p^2 X \right] \right. \tag{4.6}$$
$$\left. \cdot \left\{ \int_{Y'=0}^{1} H(\gamma_p, Y') F_{X=0}(Y')\, dY' + \int_0^X \exp\left[\left(\frac{\alpha}{U_0}\right)\gamma_p^2 X' \right] B(X')\, dX' \right\} \right),$$

where the eigenvalues $\gamma_p = p\pi$ (with $p = 1, 2, 3, \dots$) correspond to the eigenfunction $H(\gamma_p, Y) = \cos(\gamma_p Y)$ and normalization integral $1/N(\gamma_p) = 2$ [32]. Because the boundary conditions to the eigenvalue problem in the crosschannel axis (4.5) are both of Neumann type, 0 is also an eigenvalue corresponding to $H(\gamma_0, Y) = 1$ with the normalization integral $1/\ N_0 = 1$ [32]. To obtain the final expressions for fuel, oxidant, and electrolyte concentration, the general boundary condition functions in (4.5) need to be replaced with the appropriate functions, which are summarized in Table 4.1. The integrals for the inlet condition are easily evaluated, while the integrals associated with the kinetic boundary conditions cannot be evaluated until the local current density profile ($J(X)$) is known (section 5).

4.1.2. Electrolyte potential. The governing equation for the outer region electrolyte potential (4.2) cannot be solved easily by analytic techniques because of the complicated electrolyte concentration given in (4.6). Therefore, to proceed we assume the (normalized) electrolyte concentration is constant, C_{in}, for the purpose of

evaluating the electrolyte potential distribution. Although this assumption may not be justified in all cases, we find that the electrolyte potential distribution obtained using this assumption is practically identical to the electrolyte potential given by a full model (shown later). Furthermore, the boundary conditions are of Neumann type because only changes in potential are physically relevant. To obtain a solution we define an arbitrary zero potential datum: $\widehat{\Phi}_E(10L_2, Y) = 0$. The position of the arbitrary zero $(10L_2)$ is irrelevant as long as it is sufficiently far away from the electrodes. The outer problem for electrolyte potential can now be written as

$$C_{\text{in}}\frac{\partial^2\widehat{\Phi}_E^0}{\partial X^2} + C_{\text{in}}\frac{\partial^2\widehat{\Phi}_E^0}{\partial Y^2} = 0, \tag{4.7}$$

$$\begin{gathered}\frac{\partial\widehat{\Phi}_E^0}{\partial Y}(X,0) = \frac{-2S_{C^+}}{C_{\text{in}}}J_{\text{AN}}(X), \quad \frac{\partial\widehat{\Phi}_E^0}{\partial Y}(X,1) = \frac{2S_{C^+}}{C_{\text{in}}}J_{\text{CA}}(X), \\ \frac{\partial\widehat{\Phi}_E^0}{\partial X}(0,Y) = 0, \quad \widehat{\Phi}_E^0(10L_2, Y) = 0.\end{gathered} \tag{4.8}$$

Again we use the integral transform technique, which yields the solution to (4.7) [30]:

$$\begin{aligned}\widehat{\Phi}_E^0(X,Y) = \frac{-2S_{C^+}}{C_{\text{in}}}\sum_{m=1}^{\infty}\Bigg\{&\frac{G(\theta_m, X)}{\theta_m N(\theta_m)} \\ \cdot\Bigg[&\left(\sinh(\theta_m Y) - \frac{\cosh(\theta_m Y)\cosh(\theta_m)}{\sinh(\theta_m)}\right)\int_{X'=0}^{10L_2} X(\theta_m, X')\, J_{\text{AN}}(X')\, dX' \\ &-\frac{\cosh(\theta_m Y)}{\sinh(\theta_m)}\int_{X'=0}^{10L_2} X(\theta_m, X')\, J_{\text{CA}}(X')\, dX'\Bigg]\Bigg\},\end{aligned} \tag{4.9}$$

where the eigenvalues $\theta_m = (2m-1)\pi/(20L)$ (with $m = 1, 2, 3, \dots$) correspond to the eigenfunction $G(\theta_m, X) = \cos(\theta_m X)$ and normalization integral $1/N(\theta_m) = 2/10L_2$ [32]. Finally, redefining the arbitrary zero potential datum to be the midpoint of the inlet by subtracting $\widehat{\Phi}_E^0(0, 1/2)$ from the entire solution and recognizing that the integrals associated with the kinetic boundary conditions are only nonzero at positions $L_1 \le X \le L_2$, the final expression for the outer region electrolyte potential can be rewritten as

$$\begin{aligned}\widehat{\Phi}_E^0(X,Y) = \frac{-4S_{C^+}}{10L_2 C_{\text{in}}}\sum_{m=1}^{\infty}\Bigg\{&\frac{\cos(\theta_m X)}{\theta_m} \\ \cdot\Bigg[&\left(\sinh(\theta_m Y) - \frac{\cosh(\theta_m Y)\cosh(\theta_m)}{\sinh(\theta_m)}\right)\int_{L_1}^{L_2}\cos(\theta_m X')\, J_{\text{AN}}(X')\, dX' \\ &-\frac{\cosh(\theta_m Y)}{\sinh(\theta_m)}\int_{L_1}^{L_2}\cos(\theta_m X')\, J_{\text{CA}}(X')\, dX'\Bigg] + \frac{\cosh(\theta_m/2)}{\sinh(\theta_m)} \\ \cdot&\left(\int_{L_1}^{L_2}\cos(\theta_m X')\, J_{\text{CA}}(X')\, dx' + \int_{L_1}^{L_2}\cos(\theta_m X')\, J_{\text{AN}}(X')\, dx'\right)\Bigg\}.\end{aligned} \tag{4.10}$$

4.2. Inner region. The leading order approximations for the diffuse layers at the anode $(Y = 0)$ and cathode $(Y = 1)$ are obtained by rescaling the crosschannel coordinate in (3.7)–(3.10) and boundary conditions (3.11)–(3.14) to the inner

coordinates $\xi_{\mathrm{AN}} = Y/\epsilon_D$ and $\xi_{\mathrm{CA}} = (1-Y)/\epsilon_D$ for the anode and cathode, respectively. We also introduce the asymptotic expansion (where the ˜ accent denotes the asymptotic approximation in the inner region) $f(X,Y) \sim \tilde{f}(X,\xi) = \tilde{f}^0(X,\xi) + \epsilon_D \tilde{f}^1(X,\xi) + O\left({\epsilon_D}^2\right)$ and take the leading order (${\epsilon_D}^0$-order) system of equations.

Note. We have identified that the inner problems resulting from the rescaled spatial coordinates ξ_{AN} and ξ_{CA} are identical and have used a general coordinate ξ for both.

$$\frac{\partial}{\partial\xi}\left(\frac{\partial\tilde{C}_E^0(X,\xi)}{\partial\xi} + \tilde{\rho}_E^0(X,\xi)\frac{\partial\widetilde{\Phi}_E^0(X,\xi)}{\partial\xi}\right) = 0, \tag{4.11}$$

$$\frac{\partial}{\partial\xi}\left(\frac{\partial\tilde{\rho}_E^0(X,\xi)}{\partial\xi} + \tilde{C}_E^0(X,\xi)\frac{\partial\widetilde{\Phi}_E^0(X,\xi)}{\partial\xi}\right) = 0, \tag{4.12}$$

$$-\frac{\partial^2\widetilde{\Phi}_E^0(X,\xi)}{\partial^2\xi} = \tilde{\rho}_E^0(X,\xi) \tag{4.13}$$

with rescaled boundary conditions at $\xi = 0$:

$$\frac{\partial\tilde{C}_E^0}{\partial\xi} + \tilde{\rho}_E^0\frac{\partial\widetilde{\Phi}_E^0}{\partial\xi} = 0, \quad \frac{\partial\tilde{\rho}_E^0}{\partial\xi} + \tilde{C}_E^0\frac{\partial\widetilde{\Phi}_E^0}{\partial\xi} = 0, \tag{4.14}$$

$$\Phi_S = \delta\frac{\partial\widetilde{\Phi}_E^0}{\partial\xi}. \tag{4.15}$$

Finally, to fully define the inner problem we also require the matching conditions between the inner and outer solutions at the anode and cathode, respectively:

$$\lim_{\xi_{\mathrm{AN}}\to\infty}\tilde{C}_E(X,\xi) = \lim_{Y\to 0}\hat{C}_E(X,Y), \quad \lim_{\xi_{\mathrm{AN}}\to\infty}\widetilde{\Phi}_E(X,\xi) = \lim_{Y\to 0}\widehat{\Phi}_E(X,Y), \tag{4.16}$$

$$\lim_{\xi_{\mathrm{CA}}\to\infty}\tilde{C}_E(X,\xi) = \lim_{Y\to 1}\hat{C}_E(X,Y), \quad \lim_{\xi_{\mathrm{CA}}\to\infty}\widetilde{\Phi}_E(X,\xi) = \lim_{Y\to 1}\widehat{\Phi}_E(X,Y). \tag{4.17}$$

To obtain the solution for (4.11)–(4.13) and the boundary and matching conditions (4.14)–(4.17) we employ a similar approach outlined elsewhere [13], except we have allowed the constant of integration $P_{\mathrm{EL}}(X)$ to be a function of X. The expressions for the Stern potential, electrolyte concentration, charge density, and electrolyte potential are, respectively,

$$\Phi_{S,\mathrm{EL}}(X) = \mp 2\delta\sqrt{\hat{C}_{E,\mathrm{EL}}^0(X,Y_{\mathrm{EL}})}\,\mathrm{csch}\left(\sqrt{\hat{C}_{E,\mathrm{EL}}^0(X,Y_{\mathrm{EL}})}P_{\mathrm{EL}}(X)\right), \tag{4.18}$$

$$\begin{aligned}\tilde{C}_{E,\mathrm{EL}}^0(X,\xi) &= \hat{C}_{E,\mathrm{EL}}^0(X,Y_{\mathrm{EL}})\\ &\cdot\left[1 + 2\,\mathrm{csch}^2\left(\sqrt{\hat{C}_{E,\mathrm{EL}}^0(X,Y_{\mathrm{EL}})}\,(\xi + P_{\mathrm{EL}}(X))\right)\right],\end{aligned} \tag{4.19}$$

$$\begin{aligned}\tilde{\rho}_{E,\mathrm{EL}}^0(X,\xi) &= \pm 2\hat{C}_{E,\mathrm{EL}}^0(X,Y_{\mathrm{EL}})\,\mathrm{csch}\left(\sqrt{\hat{C}_{E,\mathrm{EL}}^0(X,Y_{\mathrm{EL}})}\,(\xi + P_{\mathrm{EL}}(X))\right)\\ &\cdot\coth\left(\sqrt{\hat{C}_{E,\mathrm{EL}}^0(X,Y_{\mathrm{EL}})}\,(\xi + P_{\mathrm{EL}}(X))\right),\end{aligned} \tag{4.20}$$

$$\begin{aligned}\widetilde{\Phi}_{E,\mathrm{EL}}^0(X,\xi) &= \widehat{\Phi}_{E,\mathrm{EL}}^0(X,Y_{\mathrm{EL}})\\ &\mp 4\tanh^{-1}\left(\exp\left[-\sqrt{\hat{C}_{E,\mathrm{EL}}^0(X,Y_{\mathrm{EL}})}\,(\xi + P_{\mathrm{EL}}(X))\right]\right).\end{aligned} \tag{4.21}$$

In (4.20) the upper sign (of $\pm, \mp$) refers to potentials below the point of zero charge, and $Y_{\mathrm{EL}} = 0, 1$ for the anode or cathode, respectively. The unknown constant $P_{\mathrm{EL}}(X)$ can be obtained by solving (4.18)–(4.20) along with the gFBV equations

$$\begin{aligned} J_{\mathrm{AN}}(X) = \Big[& K_F C_F(X,0) \exp\left((1-\beta)\,\Phi_{S,\mathrm{AN}}(X)\right) \\ & -K'_F \left(\tilde{C}^0_{E,\mathrm{AN}}(X,0) + \widetilde{\rho}^0_{E,\mathrm{AN}}(X,0)\right) \exp\left(-\beta \Phi_{S,\mathrm{AN}}(X)\right) \Big], \\ J_{\mathrm{CA}}(X) = \Big[& K'_O \exp\left((1-\beta)\,\Phi_{S,\mathrm{CA}}(X)\right) \\ & -K_O C_O(X,1) \left(\tilde{C}^0_{E,\mathrm{CA}}(X,0) + \widetilde{\rho}^0_{E,\mathrm{CA}}(X,0)\right) \exp\left(-\beta \Phi_{S,\mathrm{CA}}(X)\right) \Big] \end{aligned} \tag{4.22}$$

and the use of (4.6). This system of equations must be solved numerically.

5. Current density. The analytical expressions in (4.6) and (4.10) still require the specified local current density profile to be completed by evaluating the integrals associated with the kinetic boundary conditions. In this section we introduce such profiles in terms of the parameters A_1, A_2, A_3, the values of which will be evaluated later in this section and may be different for the anode and cathode. For now we present the profiles for a generic electrode:

$$\begin{aligned} &\text{Profile A: } J_{\mathrm{EL}}(X) = A_{1,\mathrm{EL}}, \\ &\text{Profile B: } J_{\mathrm{EL}}(X) = A_{1,\mathrm{EL}} - A_{2,\mathrm{EL}}(X - L_1), \\ &\text{Profile C: } J_{\mathrm{EL}}(X) = A_{1,\mathrm{EL}} - \frac{A_{2,\mathrm{EL}}}{\sqrt{X - (L_1 - A_{3,\mathrm{EL}})}}. \end{aligned} \tag{5.1}$$

Profile A is a constant current density and is analogous to using one-dimensional solutions to study the multidimensional cell. However, since fuel cells are inherently multidimensional devices, we also include profiles that allow for the current density to vary along the streamwise surface of the electrode. Profile B assumes a linearly varying current density distribution and is the simplest profile that accounts for the decay of current density along the surface of the electrode. Profile C is the most complex profile we study. It is able to describe the highly nonlinear developing region of the current density distribution near the upstream edge of the electrode. Figure 5.1 shows how the profiles compare to the local current density profile obtained from the numerical results.

The total cell current density is the controlled parameter in the galvanostatic operation of the model problem. Therefore, equivalent cell current densities are used to compare the specified profiles and numerical results appropriately. The cell current density can be calculated as the average local current density along an electrode:

$$\overline{J}_{\mathrm{Cell}} = \frac{1}{(L_2 - L_1)} \int_{L_1}^{L_2} J_{\mathrm{AN}}(X) dX = \frac{-1}{(L_2 - L_1)} \int_{L_1}^{L_2} J_{\mathrm{CA}}(X) dX, \tag{5.2}$$

where the anode current density is positive by convention and the cathode current density is negative but equal in magnitude due to the conservation of current. Since $\overline{J}_{\mathrm{Cell}}$ is the controlled parameter (and therefore the model input), a relationship between the profile parameters can be obtained by solving (5.2) for each profile. The value of the first current density profile parameter in terms of the second and third

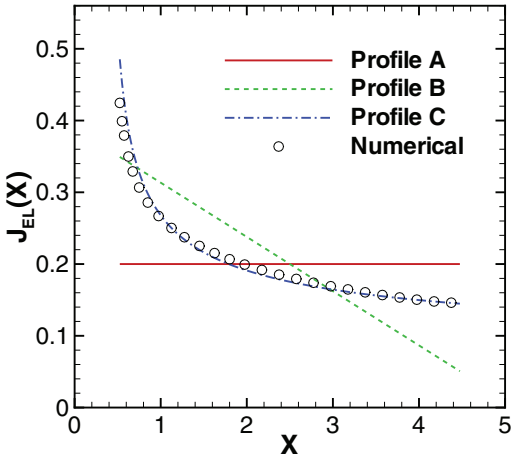

FIG. 5.1. *Specified profiles of local current density along the electrode that are considered in this study to compare with numerical results. The electrode dimensions are arbitrarily set to* $L_1 = 0.5$, $L_2 = 4.5$ *for easier comparison with numerical results.*

parameters and $\overline{J}_{\text{Cell}}$ for all profiles is

$$\text{Profile A: } A_{1,\text{EL}} = \overline{J}_{\text{Cell}},$$

$$\text{Profile B: } A_{1,\text{EL}} = \overline{J}_{\text{Cell}} + \frac{A_{2,\text{EL}}\,(L_2 - L_1)}{2}, \tag{5.3}$$

$$\text{Profile C: } A_{1,\text{EL}} = \overline{J}_{\text{Cell}} + \frac{2A_{2,\text{EL}}\left(\sqrt{A_{3,\text{EL}}} - \sqrt{L_2 - (L_1 - A_{3,\text{EL}})}\right)}{(L_2 - L_1)}.$$

We complete the description of the specified current density profile by determining how the second and third profile parameters A_2, A_3 change as total cell current density increases from short circuit to open circuit. The local current density profiles from the numerical results for different cell current densities are presented in Figure 5.2(a). The value of the current density profile parameters A_2 and A_3 with respect to $\overline{J}_{\text{Cell}}$ are calculated by minimizing the total root mean square (r.m.s.) error [33],

$$\text{Total r.m.s. error} = \left(\int_{L_1}^{L_2} \left[J_{\text{EL}}^{\text{Profile}}(X) - J_{\text{EL}}^{\text{Numerical}}(X)\right]^2 dX\right)^{1/2}, \tag{5.4}$$

between the analytical and numerical profiles. The results are then normalized by the value of the parameters at the reference condition which have been defined as $\alpha = 0.1$, $\delta = 0.1$, $U_0 = 60$, $L_2 = 4.5$, $K_{\text{EL}} = 1$, $K'_{\text{EL}} = 10^{-4}$, $S_{C^+} = 2$, and $\overline{J}_{\text{Cell}} = 0.1$. The values for the reference condition parameters are presented in Table 5.1. To describe the parameters for all values of $\overline{J}_{\text{Cell}}$ a best fit relationship is developed in Figure 5.2(b). The constitutive equations for the normalized parameters with respect to cell current density for the anode (AN) and cathode (CA) are

$$\frac{A_{2,\text{AN}}\left(\overline{J}_{\text{Cell}}\right)}{A_{2,\text{AN}}^{\text{Ref}}} = 80.46\overline{J}_{\text{Cell}}{}^2, \quad \frac{A_{2,\text{CA}}\left(\overline{J}_{\text{Cell}}\right)}{A_{2,\text{CA}}^{\text{Ref}}} = 142.04\overline{J}_{\text{Cell}}{}^2, \tag{5.5}$$

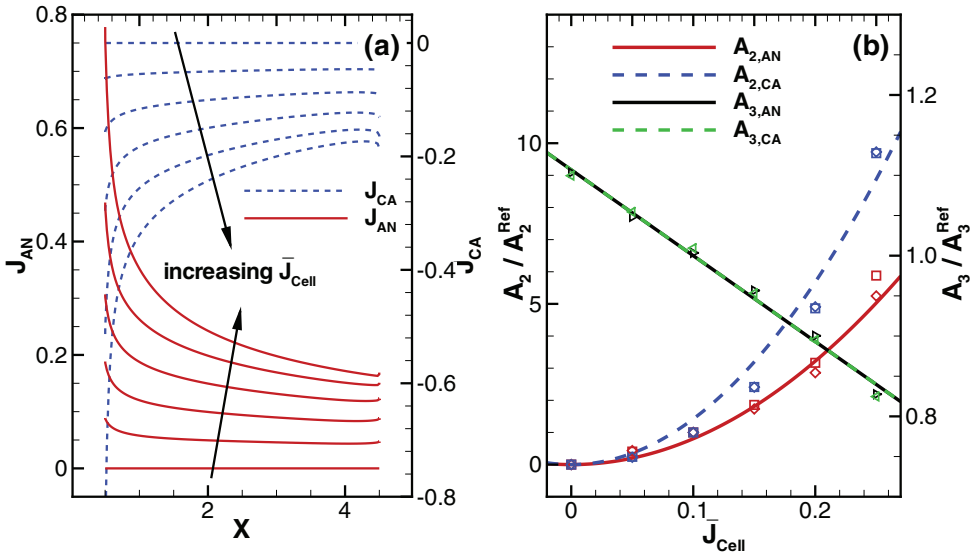

FIG. 5.2. (a) *Local current density profiles along the anode and cathode for various values of total cell current density* $\left(0 \leq \overline{J}_{Cell} \leq 0.25\right)$ *from numerical results. The other operating conditions are maintained at the reference condition.* (b) *Normalized parameters for the specified local current density profiles (□: Profile B, ◇: Profile C) and the best fit curves for the parameters with respect to total cell current density. The parameters are normalized by the reference condition parameters. The reference conditions have been defined as* $\alpha = 0.1$, $\delta = 0.1$, $U_0 = 60$, $L_1 = 0.5$, $L_2 = 4.5$, $K_{EL} = 1$, $K'_{EL} = 10^{-4}$, $S_{C+} = 2$, *and* $\overline{J}_{Cell} = 0.1$.

TABLE 5.1
Reference parameters.

	$A^{\text{Ref}}_{2,\text{AN}}$	$A^{\text{Ref}}_{2,\text{CA}}$	$A^{\text{Ref}}_{3,\text{AN}}$	$A^{\text{Ref}}_{3,\text{CA}}$
Profile A	-	-	-	-
Profile B	0.0210	0.0145	-	-
Profile C	-0.0425	-0.0220	0.1167	0.0780

$$\frac{A_{3,\text{AN}}\left(\overline{J}_{\text{Cell}}\right)}{A^{\text{Ref}}_{3,\text{AN}}} = \frac{A_{3,\text{CA}}\left(\overline{J}_{\text{Cell}}\right)}{A^{\text{Ref}}_{3,\text{CA}}} = 1.11 - 1.07\overline{J}_{\text{Cell}}. \tag{5.6}$$

6. Cell potential. The total cell potential must be recovered in order to generate fuel cell performance data from (4.6), (4.10), and (4.21). In this section we develop analytic expressions for the electrode potential distributions and total cell potential as well as present LFFC performance plots for all current density profiles. The average cell potential, $\overline{\Psi}_{\text{Cell}}$, can be calculated as

$$\overline{\Psi}_{\text{Cell}} = \frac{1}{(L_2 - L_1)} \int_{L_1}^{L_2} \Psi_{\text{Cell}}(X) dX, \tag{6.1}$$

where the cell potential profile along the channel, $\Psi_{\text{Cell}}(X)$, is given by

$$\Psi_{\text{Cell}}(X) = \Psi_{\text{CA}}(X) - \Psi_{\text{AN}}(X) \tag{6.2}$$

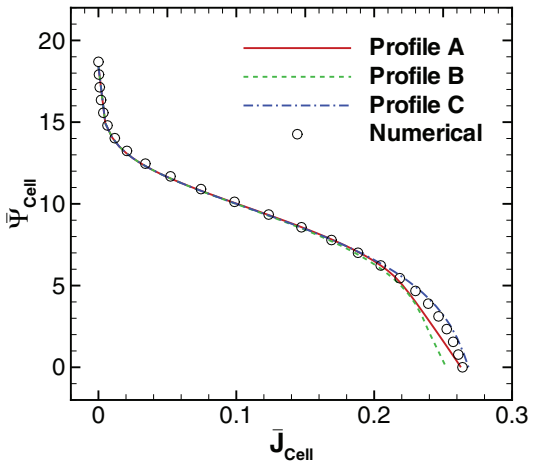

FIG. 6.1. *Device performance (V-I curve) of the LFFC. All the analytic profiles are considered and compared against numerical results. The operating conditions are* $\alpha = 0.1$, $\delta = 0.1$, $U_0 = 60$, $L_1 = 0.5$, $K_{EL} = 1$, $K'_{EL} = 10^{-4}$, $S_{C^+} = 2$, *and* $L_2 = 4.5$.

and the electrode potentials ($\Psi_{\mathrm{EL}}(X)$) are equal to the Stern potential ($\Phi_S(X)$) plus the electrolyte potential ($\widetilde{\Phi}^0_E(X)$) at the reaction plane:

$$\begin{aligned} \Psi_{\mathrm{CA}}(X) &= \Phi_{S,\mathrm{CA}}(X) + \widetilde{\Phi}^0_{E,\mathrm{CA}}(X,0), \\ \Psi_{\mathrm{AN}}(X) &= \Phi_{S,\mathrm{AN}}(X) + \widetilde{\Phi}^0_{E,\mathrm{AN}}(X,0). \end{aligned} \tag{6.3}$$

Evaluating (4.6), (4.10), and (6.1) for values of $\overline{J}_{\mathrm{Cell}}$ ranging from short circuit to open circuit yields the cell performance results presented in Figure 6.1 for all profiles. Figure 6.1 shows the total cell performance compared to the numerical results. At the device level all profiles provide reasonably accurate descriptions of the model problem. The fact that even the simple specified current density profiles still provide accurate device level results is not unexpected because the cell current and cell potential are integral averages (see (5.2) and (6.1)). Therefore, a reasonable description of the device behavior can be obtained without an accurate description of the local conditions along the electrode. The ability to obtain system level information without detailed knowledge of the continuum distributions is a well-known result of integral analysis.

7. Spatial distributions. One of the primary strengths of mathematical studies of physical systems is the ability to probe quantities that cannot be measured experimentally. Therefore, while it is imperative that the device level results are accurate, our solution must also describe the spatial distributions accurately. In this section we study these distributions and evaluate the validity of the analytical solution against the numerical simulation of the complete model problem.

7.1. Outer region solutions. In developing our analytical expressions to describe the LFFC we divided the domain into three regions—the outer region and the anode and cathode diffuse regions under the thin double layer assumption. We then solved the outer region problem where the charge density was zero at leading order. To evaluate the accuracy of this approach the outer region solutions (4.6) and (4.10) are compared to the numerical results outside the diffuse region ($Y = 4\lambda_D$) along

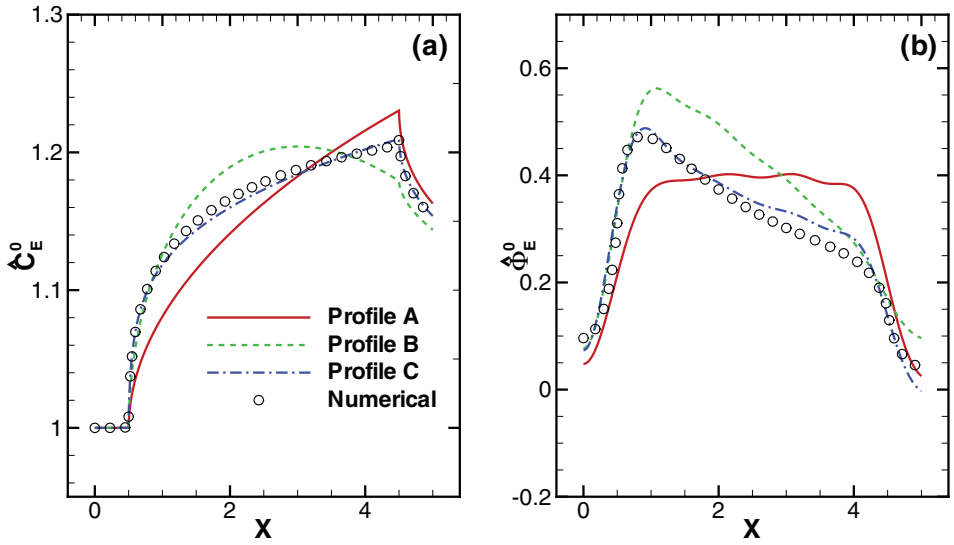

FIG. 7.1. *Outer region distributions for* (a) *electrolyte concentration and* (b) *electrolyte potential along the interface between the inner and outer regions of the anode for all specified profiles of local current density. The analytic distributions are compared to the distributions just outside the diffuse region,* $Y = 4\lambda_D$*, obtained from the numerical results. The operating conditions are* $\alpha = 0.1$*,* $\delta = 0.1$*,* $U_0 = 60$*,* $L_1 = 0.5$*,* $L_2 = 4.5$*,* $K_{EL} = 1$*,* $K'_{EL} = 10^{-4}$*,* $S_{C+} = 2$*, and* $\overline{J}_{Cell} = 0.2$*.*

the anode. Figure 7.1(a) shows the electrolyte concentration along the anode for all profiles. The electrolyte potential is shown in Figure 7.1(b). It can be seen that while all the profiles provide reasonable results, only profile C accurately describes the physical distributions along the electrode. Additionally, even though in the derivation of the analytical expression for electrolyte potential (section 4.1.2) we assume that the electrolyte concentration is constant, the distribution obtained is still accurate as shown in Figure 7.1(b). The distributions along the interface between the inner and outer regions are especially important because these results strongly influence the inner region results due to the matching conditions in (4.16) and (4.17).

7.2. Electrode distributions. The model problem considers galvanostatic operation, and therefore the electrode potential must be recovered from the solution (section 6). This places a further restriction on the local current density profile because in reality the electrode potential should remain constant along the electrode. This is because the resistance of the metallic electrode (e.g., gold) is significantly lower than the equivalent resistance of the electrolyte. Therefore, any difference in local current density must be accommodated by changes in the electrolyte potential and not the electrode potential. The electrode and Stern potential distributions are presented in Figures 7.2(a) and 7.2(b), respectively, for both electrodes. Here the numerical results correspond to the physically realistic distribution of the electrode potentials. It can be seen that only profile C yields acceptable results. The other profiles provide electrode potential distributions that are physically unfeasible. Therefore, at this point we proceed only with profile C for the remainder of our analysis.

7.3. Continuum distributions. It is paramount that the predefined local current density profile yields accurate results throughout the continuum domain for other

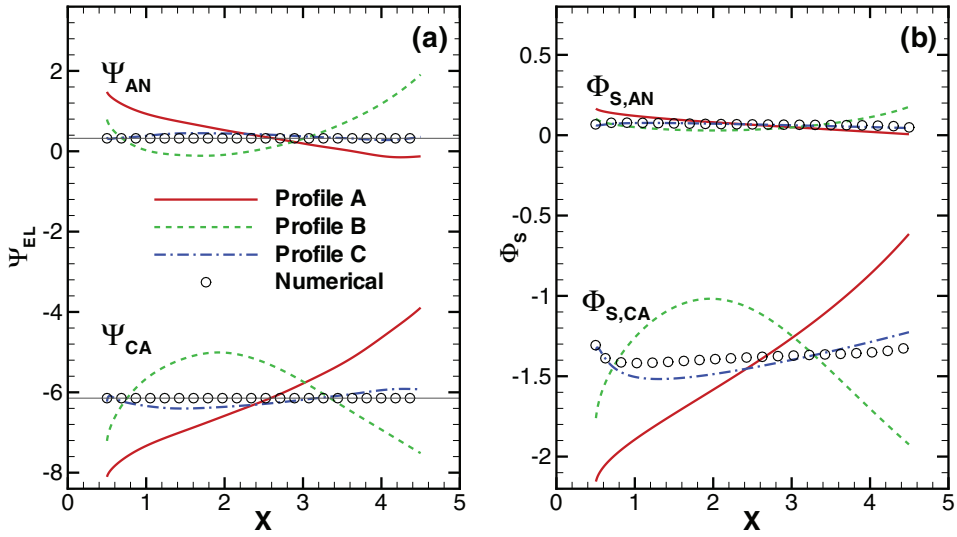

FIG. 7.2. (a) *Electrode potential and* (b) *Stern potential distributions along the anode and cathode for all specified local current density profiles compared to numerical results. The operating conditions are* $\alpha = 0.1$, $\delta = 0.1$, $U_0 = 60$, $L_1 = 0.5$, $L_2 = 4.5$, $K_{EL} = 1$, $K'_{EL} = 10^{-4}$, $S_{C+} = 2$, *and* $\overline{J}_{Cell} = 0.2$.

variables such as species concentration and electrolyte potential. Figure 7.3 shows the crosschannel distributions of the continuum electrolyte quantities at different positions along the channel. The results are presented for all three domains (left panel = anode diffuse region, center panel = bulk region, right panel = cathode diffuse region) along with the numerical results from the full PNP model. Figure 7.3(a) shows the electrolyte concentration. It can be seen that the analytical solution agrees very well with the numerical solution. The electrolyte potential in Figure 7.3(b) also agrees quite well with the numerical solution but with slight deviations. Careful inspection reveals that the error is in the Ohmic drop across the bulk electrolyte. In fact, in the inner regions, the analytical electrolyte potential distributions are merely offset from the numerical solutions by the deviation present at the boundaries of the outer region. This indicates that, while the inner distributions are correct, the matching conditions derived the from the outer region solution introduce some minor error. It is likely that this deviation in the outer region is due to the approximation of the constant electrolyte concentration in our derivation of (4.10) (section 4.1.2). The full equation (3.8) shows that the concentration gradients could affect the diffusion of the electrolyte potential. However, the crosschannel average of electrolyte concentration is constant along the streamwise direction of the fuel cell. Therefore, this deviation is not significant, and the solutions presented are still relevant.

The analytical solutions presented in this work match well with numerical simulations of the full model problem. An excellent agreement between these two methods validates the *thin double layer* assumption and the application of asymptotic analysis in multidimensional fuel cell studies. In studying the resulting solutions, we demonstrated that overall device performance results can be obtained through grossly simplified descriptions, while spatial distributions require a very specific local current

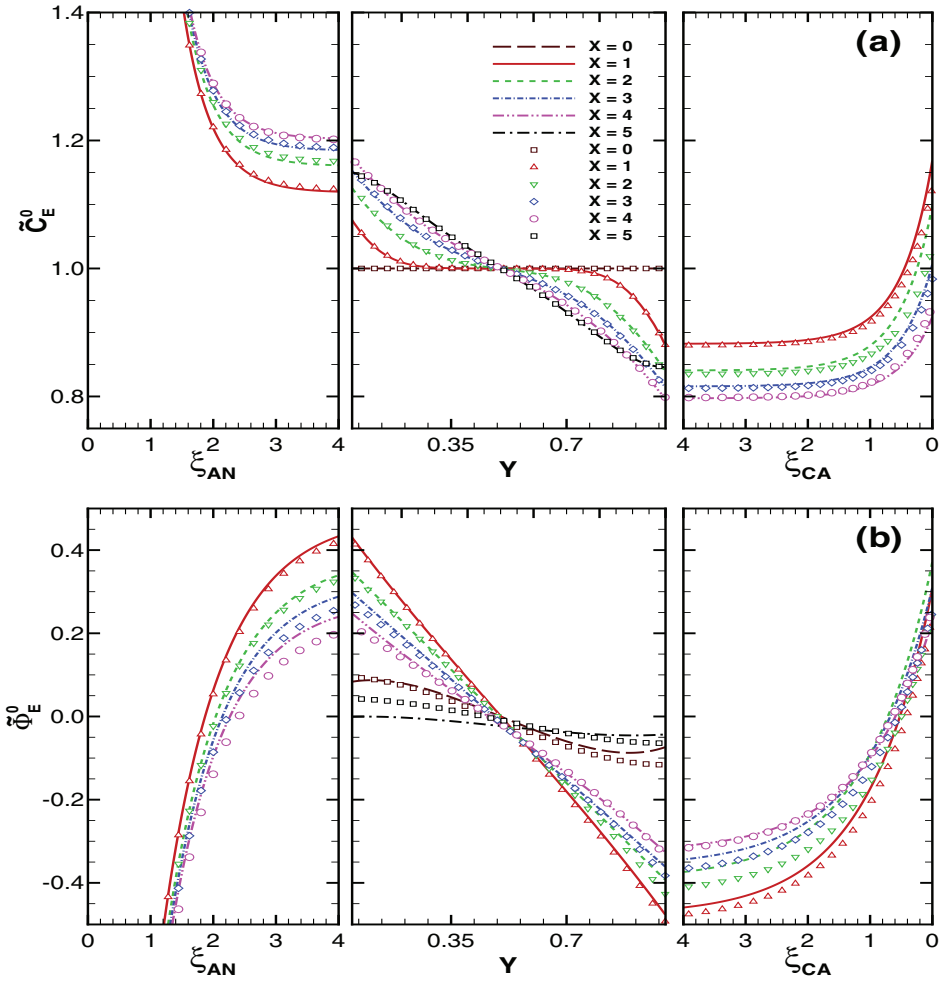

FIG. 7.3. *Crosschannel distributions for* (a) *electrolyte concentration and* (b) *electrolyte potential throughout the entire continuum domain at different positions along the channel. The analytical results from specified local current density profile C are compared to numerical results and presented for the three different regions (left panel: anode diffuse layer; center panel: bulk region; right panel: cathode diffuse layer). The operating conditions are* $\alpha = 0.1$, $\delta = 0.1$, $U_0 = 60$, $L_1 = 0.5$, $L_2 = 4.5$, $K_{EL} = 1$, $K'_{EL} = 10^{-4}$, $S_{C^+} = 2$, *and* $\overline{J}_{Cell} = 0.2$.

density profile. The presented analysis helps to show that the electrode-electrolyte interface structure is readily accessible through the gFBV–PNP equations and the use of thin double layer approximations. The advantage of the analytical solution is that practical devices (whose physical domains may be too large or computationally prohibitive to simulate) can be quickly described mathematically allowing for matching of the numerous model parameters to empirical results without the omission of the EDL.

Additionally, the inner region problems resulting from the asymptotic expansion were one-dimensional along the electrode normal. Only the matching conditions imposed from the outer region varied along the streamwise direction. This suggests that simple EDL coupled kinetic behavior of electrochemical devices can easily be included

in complex multidimensional device analyses by matching the inner solutions to the outer region continuum variables at the boundaries. This allows us to study EDL affected kinetics in complex devices whose overall architecture may have prohibited full numerical simulation. However, there may be cases where the inner region physics are perturbed by outer region physics, such as in nano-porous electrodes. Nevertheless, the presented analytic model has the ability to capture EDL dependent kinetics in electrochemical devices whose spacing between electrodes is significantly greater than the diffuse layer width (*thin double layers*), such as LFFCs.

REFERENCES

[1] A. Biyikoglu, *Review of proton exchange membrane fuel cell models*, Int. J. Hydrogen Energ., 30 (2005), pp. 1181–1212.

[2] D. Cheddie and N. Munroe, *Review and comparison of approaches to proton exchange membrane fuel cell modeling*, J. Power Sources, 147 (2005), pp. 72–84.

[3] J. O'M. Bockris, A. K. N. Reddy, and M. E. Gamboa-Aldeco, *Modern Electrochemistry*, Plenum Press, New York, 1998, pp. 1068.

[4] M. Z. Bazant, K. Thornton, and A. Ajdari, *Diffuse-charge dynamics in electrochemical systems*, Phys. Rev. E, 70 (2004), 021506.

[5] A. A. Franco, P. Schott, C. Jallut, and B. Maschke, *A dynamic mechanistic model of an electrochemical interface*, J. Electrochem. Soc., 153 (2006), pp. A1053–A1061.

[6] B. Li, B. Z. Lu, Z. M. Wang, and J. A. McCammon, *Solutions to a reduced Poisson-Nernst-Planck system and determination of reaction rates*, Phys. A, 389 (2010), pp. 1329–1345.

[7] W. D. Murphy, J. A. Manzanares, S. Mafe, and H. Reiss, *A numerical study of the equilibrium and nonequilibrium diffuse double-layer in electrochemical-cells*, J. Phys. Chem., 96 (1992), pp. 9983–9991.

[8] P. M. Biesheuvel, A. A. Franco, and M. Z. Bazant, *Diffuse charge effects in fuel cell membranes*, J. Electrochem. Soc., 156 (2009), pp. B225–B233.

[9] A. A. Franco, P. Schott, C. Jallut, and B. Maschke, *A multi-scale dynamic mechanistic model for the transient analysis of PEFCs*, Fuel Cells, 7 (2007), pp. 99–117.

[10] I. B. Sprague and P. Dutta, *Modeling of diffuse charge effects in a microfluidic based laminar flow fuel cell*, Numer. Heat Tr. A-Appl., 59 (2011), pp. 1–27.

[11] I. B. Sprague, D. Byun, and P. Dutta, *Effects of reactant crossover and electrode dimensions on the performance of a microfluidic based laminar flow fuel cell*, Electrochim. Acta, 55 (2010), pp. 8579–8589.

[12] I. B. Sprague and P. Dutta, *Role of the diffuse layer in acidic and alkaline fuel cells*, Electrochim. Acta, 56 (2011), pp. 4518–4525.

[13] A. Bonnefont, F. Argoul, and M. Z. Bazant, *Analysis of diffuse-layer effects on time-dependent interfacial kinetics*, J. Electroanal. Chem., 500 (2001), pp. 52–61.

[14] M. van Soestbergen, P. M. Biesheuvel, and M. Z. Bazant, *Diffuse-charge effects on the transient response of electrochemical cells*, Phys. Rev. E, 81 (2010), 021503.

[15] M. Z. Bazant, K. T. Chu, and B. J. Bayly, *Current-voltage relations for electrochemical thin films*, SIAM J. Appl. Math., 65 (2005), pp. 1463–1484.

[16] K. T. Chu and M. Z. Bazant, *Electrochemical thin films at and above the classical limiting current*, SIAM J. Appl. Math., 65 (2005), pp. 1485–1505.

[17] G. Richardson and J. R. King, *Time-dependent modelling and asymptotic analysis of electrochemical cells*, J. Engrg. Math., 59 (2007), pp. 239–275.

[18] A. A. Sonin and R. F. Probstein, *A hydrodynamic theory of desalination by electrodialysis*, Desalination, 5 (1967), pp. 293–329.

[19] M. van Soestbergen, P. M. Biesheuvel, R. T. H. Rongen, L. J. Ernst, and G. Q. Zhang, *Modified Poisson-Nernst-Planck theory for ion transport in polymeric electrolytes*, J. Electrostat., 66 (2008), pp. 567–573.

[20] R. Ferrigno, A. D. Stroock, T. D. Clark, M. Mayer, and G. M. Whitesides, *Membraneless vanadium redox fuel cell using laminar flow*, J. Amer. Chem. Soc., 124 (2002), pp. 12930–12931.

[21] E. R. Choban, L. J. Markoski, A. Wieckowski, and P. J. A. Kenis, *Microfluidic fuel cell based on laminar flow*, J. Power Sources, 128 (2004), pp. 54–60.

[22] E. Kjeang, N. Djilali, and D. Sinton, *Microfluidic fuel cells: A review*, J. Power Sources, 186 (2009), pp. 353–369.

[23] M. H. Chang, F. Chen, and N. S. Fang, *Analysis of membraneless fuel cell using laminar flow in a y-shaped microchannel*, J. Power Sources, 159 (2006), pp. 810–816.
[24] R. S. Jayashree, S. K. Yoon, F. R. Brushett, P. O. Lopez-Montesinos, D. Natarajan, L. J. Markoski, and P. J. A. Kenis, *On the performance of membraneless laminar flow-based fuel cells*, J. Power Sources, 195 (2010), pp. 3569–3578.
[25] A. E. Khabbazi, A. J. Richards, and M. Hoorfar, *Numerical study of the effect of the channel and electrode geometry on the performance of microfluidic fuel cells*, J. Power Sources, 195 (2010), pp. 8141–8151.
[26] E. Kjeang, R. Michel, D. A. Harrington, N. Djilali, and D. Sinton, *A microfluidic fuel cell with flow-through porous electrodes*, J. Amer. Chem. Soc., 130 (2008), pp. 4000–4006.
[27] I. B. Sprague, P. Dutta, and S. Ha, *Characterization of a membraneless direct-methanol micro fuel cell*, I. Mech. Eng. A-J. Pow., 223 (2009), pp. 799–808.
[28] I. B. Sprague, P. Dutta, and S. Ha, *Flow rate effect on methanol electro-oxidation in a microfluidic laminar flow system*, J. New Mat. Elect. Syst., 13 (2010), pp. 305–313.
[29] E. Kjeang, J. McKechnie, D. Sinton, and N. Djilali, *Planar and three-dimensional microfluidic fuel cell architectures based on graphite rod electrodes*, J. Power Sources, 168 (2007), pp. 379–390.
[30] I. B. Sprague, *Mathematical Studies of the Electric Double Layer in Electrochemical Cells with an Emphasis on Laminar Flow Fuel Cells*, Ph.D. dissertation, Washington State University, Pullman, WA, 2011.
[31] H. Lin, B. D. Storey, and J. G. Santiago, *A depth-averaged electrokinetic flow model for shallow microchannels*, J. Fluid Mech., 608 (2008), pp. 43–70.
[32] M. Necati Özişik, *Heat Conduction*, 2nd ed., Wiley, New York, 1993.
[33] J. H. Mathews and K. D. Fink, *Numerical Methods Using MATLAB*, 3rd ed., Prentice–Hall, Upper Saddle River, NJ, 1999.